

## MOLECULAR DYNAMICS MODELING OF NANOSECOND LASER ABLATION: SUBCRITICAL REGIME

V.I. MAZHUKIN<sup>2,3</sup>, A.V. SHAPRANOV<sup>2,3</sup>, M.M. DEMIN<sup>2</sup>,  
A.A. SAMOKHIN<sup>1</sup>, A.E. ZUBKO<sup>1</sup>

<sup>1</sup>A.M. Prokhorov General Physics Institute, RAS, Moscow, Russia  
e-mail: asam40@mail.ru, web page: <http://www.gpi.ru/eng/>

<sup>2</sup>Keldysh Institute of Applied Mathematics, RAS, Moscow, Russia  
e-mail: vim@modhef.ru, web page: <http://www.keldysh.ru/>

<sup>3</sup>National Research Nuclear University "MEPhI", Moscow, Russia  
web page: <https://mephi.ru/eng/>

**Summary.** Nanosecond laser ablation regime is investigated for the case of thin liquid Al film heated with constant radiation intensity  $I = 33\text{MW/cm}^2$ . The film dimensions are  $x \times y \times z = 448.7 \times 37.3 \times 37.3 \text{ nm}^3$  with periodically boundary conditions in  $y$ - $z$  directions. The results of molecular dynamics modeling show four repetitive explosive boilings during laser action (5.6 ns) with attained maximum sample temperature 7000 K and recoil pressure 800 bar compared with calculated critical temperature 7630 K and critical pressure 1415 bar.

### 1 INTRODUCTION

Theoretical investigation of nanosecond laser ablation with the help of molecular dynamics modeling (MDM) is an active research field for about two last decades (see [1-17] and refs. therein). The MDM method is the only possible approach to analyze strongly non-equilibrium condensed matter behavior in near-critical region. In most papers [4-10] laser ablation is considered for femtosecond radiation pulses. In such cases as well as in ref. [11] no sufficient information about development of explosive boiling process including the corresponding pressure behavior was given.

In ref. [12-17] results of MDM calculations were presented for the case of thin liquid Al film irradiated with nanosecond laser pulses at different constant intensities permitting to analyze condensed matter behavior in near-critical region. The total particle number involved was  $N = 5 \cdot 10^5$  for the sample  $x \times y \times z = 430 \times 6.2 \times 6.2 \text{ nm}^3$  with periodical boundary condition in  $y$ ,  $z$  directions. In the present paper the sample dimensions are  $x \times y \times z = 448.7 \times 37.3 \times 37.3 \text{ nm}^3$  with the total particle number  $N = 17.87 \cdot 10^6$  and the constant laser intensity  $I = 33\text{MW/cm}^2$ .

### 2 STATEMENT OF THE PROBLEM

The metal film is considered as a combination of two interacting subsystems consisting respectively of the conduction electrons and the lattice ions with energy exchange between them [18-20]. This means that in general the subsystems are not in equilibrium with each other, for example, they may have different temperatures at the same point in space. Such an approach has been proposed previously to describe the spin systems in solids [21], the electronic and ionic subsystems in gas plasma [22].

**2010 Mathematics Subject Classification:** 97M20, 82C26, 82C27, 82D80.

**Key words and Phrases:** Evaporation, Explosive boiling, Critical point, Nanosecond laser, Molecular dynamics, Phase transformations

Laser radiation propagates from right to left and is normally incident on the free surface of the film. Part of the radiation is absorbed by the electronic components, and as a result of inelastic collisions is transferred to the ion subsystem. By using periodic boundary conditions in the directions Y, Z the problem is effectively reduced to one-dimensional approximation along the X direction (for transport processes of laser radiation and energy into electronic subsystem).

Combined TTM-MD [4] model is used to describe the processes.

Energy balance of electron subsystem is described by continuum energy equation (1) supplemented by the equation of laser radiation transfer (2):

$$\frac{\partial \varepsilon_e}{\partial t} = - \left( \frac{\partial W_e}{\partial x} + g(T_e)(T_e - T_i) + \frac{\partial G}{\partial x} \right) \quad (1)$$

$$\frac{\partial G}{\partial x} + \alpha G = 0 \quad (2)$$

Here  $\varepsilon_e$  is the volume density of electron energy,  $T_e, T_i$  are the electron and ion temperatures,  $g(T_e)$  is the electron-ion coupling coefficient,  $G$  is the density of laser radiation flux in the medium,  $\alpha = \alpha(T_e, n_e)$  is the coefficient of absorption of laser radiation,  $W_e = -\lambda_e \frac{\partial T_e}{\partial x}$  is the heat flux,  $\lambda_e(T_e, T_i)$  is the electron heat conductivity coefficient.

The energy balance equation of the electron subsystem (1) was solved in the condensed medium using the finite-difference method. Zero heat flux  $W_e = 0$  was used as a boundary condition at the surface of the film and its fragments.

The connection between electron energy and temperature was obtained using approximation via Fermi integrals [23].

3D molecular-dynamic modeling was used to describe the ion motion:

$$\begin{cases} \frac{d\vec{r}_j}{dt} = \vec{v}_j \\ m_j \frac{d\vec{v}_j}{dt} = \vec{F}_j^{emb} + \vec{F}_j^{heat} \\ j = 1 \dots N \end{cases} \quad (3)$$

Here  $m_j, \vec{r}_j, \vec{v}_j$  are the mass, radius-vector and velocity of j-th ion respectively,  $\vec{F}_j^{emb} = -\frac{\partial U(\vec{r}_1 \dots \vec{r}_N)}{\partial \vec{r}_j}$  is the force acting at the j-th ion from other ions,  $U(\vec{r}_1 \dots \vec{r}_N)$  is the interaction potential for which embedded atom model (EAM) potential [24] was chosen. The energy transfer from the electron subsystem to the ion is given by:

$$\vec{F}_j^{heat} = \frac{m_j(\vec{v}_j - \langle \vec{v} \rangle)}{3k_B T_i n_i} g(T_e)(T_e - T_i), \quad (4)$$

where  $\langle \vec{v} \rangle$  is the mean ion velocity in the neighborhood of the j-th ion.

At the initial time  $t = 0$  the film was assumed to be heated to the temperature of 6340K, electron and ion subsystems are in thermal equilibrium.

### 3 RESULTS AND DISCUSSION

Behavior of the heated films parameters is shown in figs 1-26 at constant laser intensity at  $I = 33\text{MW/cm}^2$ . Initial state of the film at  $t = 0$  ps is prepared at  $T(t=0) = 6340$  K with no evaporation and  $P(t=0) = 0$  bar. In this figs cases (a,b,c,d) present 1D distributions (averaged over z-y directions) of temperature  $T$ , density  $\rho$ , pressure  $P$ , particle velocity  $U$  respectively in the film and vapor. Snapshot (e) shows 2D density particle distribution (averaged over y direction) in the whole  $x$ -calculation domain.

Effect of laser heating of the right hand film side is already evident at  $t = 15$  ps after the irradiation is switched on in fig.1 where the right side (RS) film pressure due to vaporization (recoil) pressure exceeds the pressure on the left (back) side  $P_L$ . At RS temperature  $T_R = 6450$  K (fig.2a) saturated pressure is about  $P_S = 500$  bar and the recoil pressure  $P_R \approx 0.6 P_S = 300$  bar, which is in qualitative agreement with fig.2c. It should be mentioned that in the considered scale there is no visible difference between temperature values at the surface  $T_R$  and at the location of the subsurface temperature maximum  $T_M$ .

Fig.3-4 show pressure vibrations in the film with maximum and minimum of pressure values in the middle of the film. Assuming that the time difference between fig. 4 and 3 is equal to a half period  $\tau$  of this vibration one can estimate sound velocity in the film with the help of the relation  $c = l/\tau = 450\text{nm}/315\text{ps} = 1430$  m/s. Approximately the same value for sound velocity is obtained from the propagation pressure maximum  $P_M$  into the sample from its RS,  $c = \Delta x/\Delta t = 62\text{nm}/45\text{ps} = 1380$  m/s, where  $\Delta x$  is the distance of the  $P_M$  from the surface in fig.2.

At fig.5 one has  $T_R = 6920$  K and pressure  $P_R = 370$  bar,  $T_L = 6420$  K and pressure  $P_L = 200$  bar. At this moment (1590 ps) density fluctuations which are also visible in fig.3b,4b begin to grow on the film RS at the depth of about 20 nm. This fluctuation growth gives rise to explosive boiling which is visible in fig.6 as density drop and pressure rise at the film RS. The resulting fragment thickness then increases due to its density decreasing (fig.6b).

During the explosive boiling the  $P_R$  rises approximately from 370 bar (fig.5c) to 550 bar (fig.6c) while the temperature remains almost the same (figs 5c, 6c). To be more precise the temperature at  $t = 1740$  ps (fig.6c) is somewhat lower than at  $t = 1590$  (fig.5c). This slight temperature decreasing is due to explosive boiling beginning which in continual approach is characterized as heat capacity singular behavior.

Fig.7-10 show ablation process evolution between the first and the second explosion. From fig.7-8 one can estimate fragment velocities  $V = \Delta x/\Delta t = 240$  m/s at  $\Delta x = 33$  nm,  $\Delta t = 135$  ps for moment  $t = 2025$  ps and  $V = 380$  m/s for  $t = 1875$  ps. Maximum pressure value  $P_M \approx 740$  bar in fig.8 ( $t = 2025$  ps) is determined probably the pressure vibrations inside the sample which were already mentioned above.

Fig.9-10 show that irradiated (RS) surface of the sample is not as flat as its left surface. The pimple visible in fig.10 (2D snapshot) then explodes as it is seen from fig.11 and the explosion gives rise to augmentation of  $P_R$  from 480 bar ( $t = 2415$  ps) to 580 bar ( $t = 2535$  ps). Pressure increasing continues (fig.12c-17c) up to about  $P_R \approx 700$  bar (fig.17,  $t = 2940$  ps) which is somewhat lower than saturated pressure  $P_S(T) \approx 800$  bar at  $T = 6950$  K (fig.17a). Maximum pressure increasing inside the sample in fig.13-15 is due to the same reason as in

fig.8. Internal pressure vibrations are visible also in fig.17-20. Estimations of the fragment velocities from fig.17-20 give  $V = 100$  m/s,  $410$  m/s,  $520$  m/s,  $690$  m/s respectively. Initial thickness of the fragment forming in the second explosion is higher than in the first explosion as it is seen from comparison of fig.10-14 and fig.5-6. It is probable that relatively large interval between the second and the third explosions is due to laser radiation absorption in the formed thick fragment.

After the second explosion the recoil pressure decreases from 700 bar to about  $P_R = 400$  bar at  $t = 4170$  ps just before the third explosion begins to develop. The third explosion (fig.22) occurs at  $t = 4545$  ps with pressure jump from  $P_R = 500$  bar ( $t = 4230$  ps) at fig.21 to  $P_R = 700$  bar at fig.22. The pressure begins to rise approximately at  $t = 4320$  ps. In fig.22 one can also see the forth explosion initiation as an additional drop in density distribution. Figs 23-24 show the forth explosion development where the attained pressure maximum is the same as in third explosion  $P_M \sim P_R$  ( $t = 4995$  ps). Recoil pressure decreasing after the forth explosion are shown in fig.25-26. The recoil pressure maximum  $P_R$  in all explosions is lower than the saturated pressure  $P_S(T_R)$ .

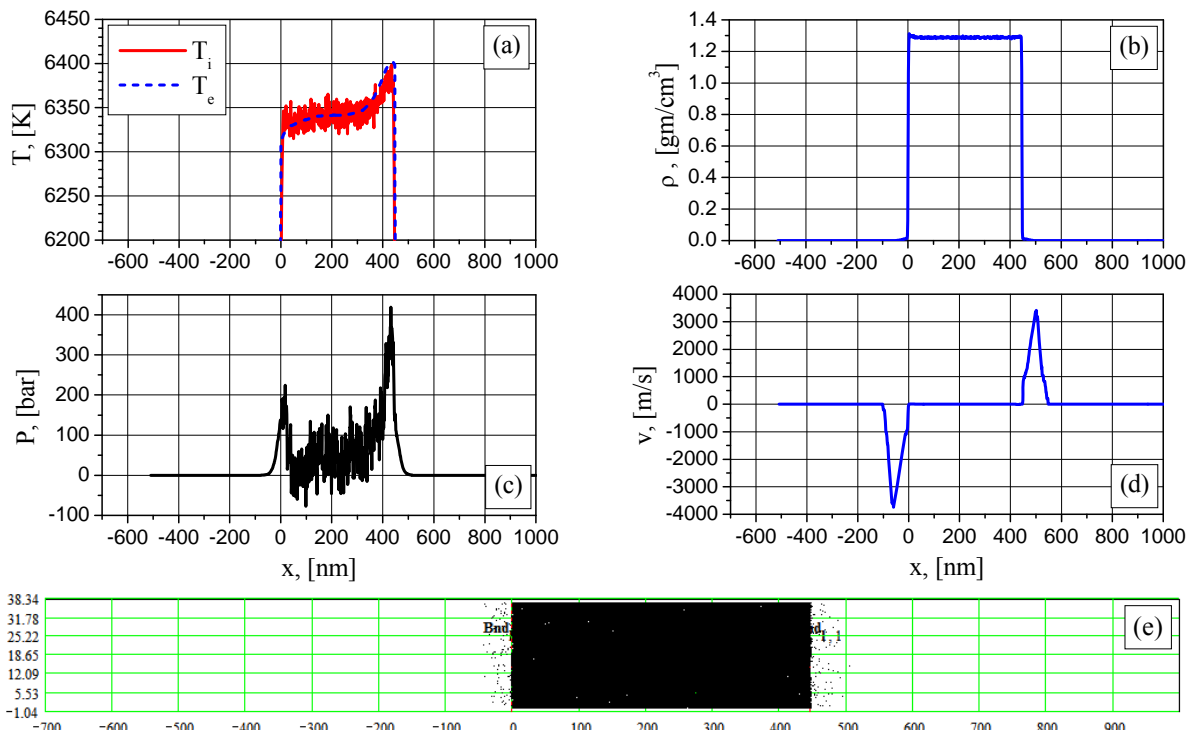


Figure 1: 1D distributions of electron (blue) and ion (red) temperature (a), density (b), pressure (c), particle velocity (d) and 2D density particle distribution (snapshot) at the time 15 ps

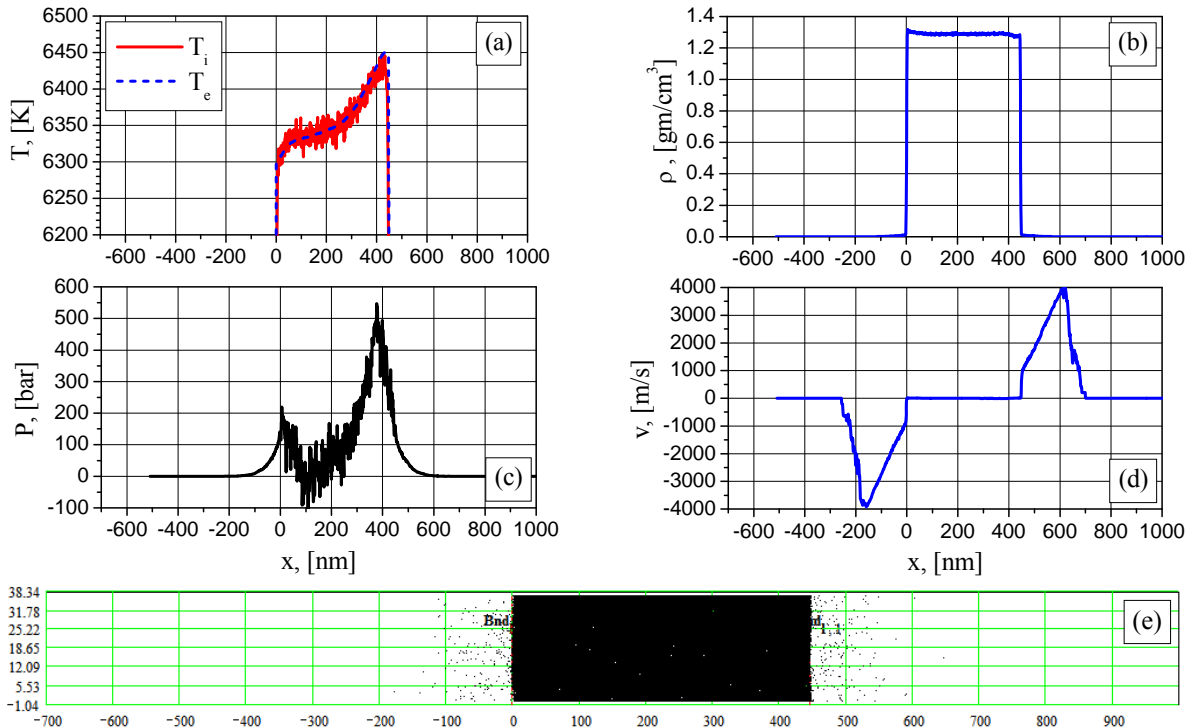


Figure 2: 1D distributions of electron (blue) and ion (red) temperature (a), density (b), pressure (c), particle velocity (d) and 2D density particle distribution (snapshot) at the time 45 ps

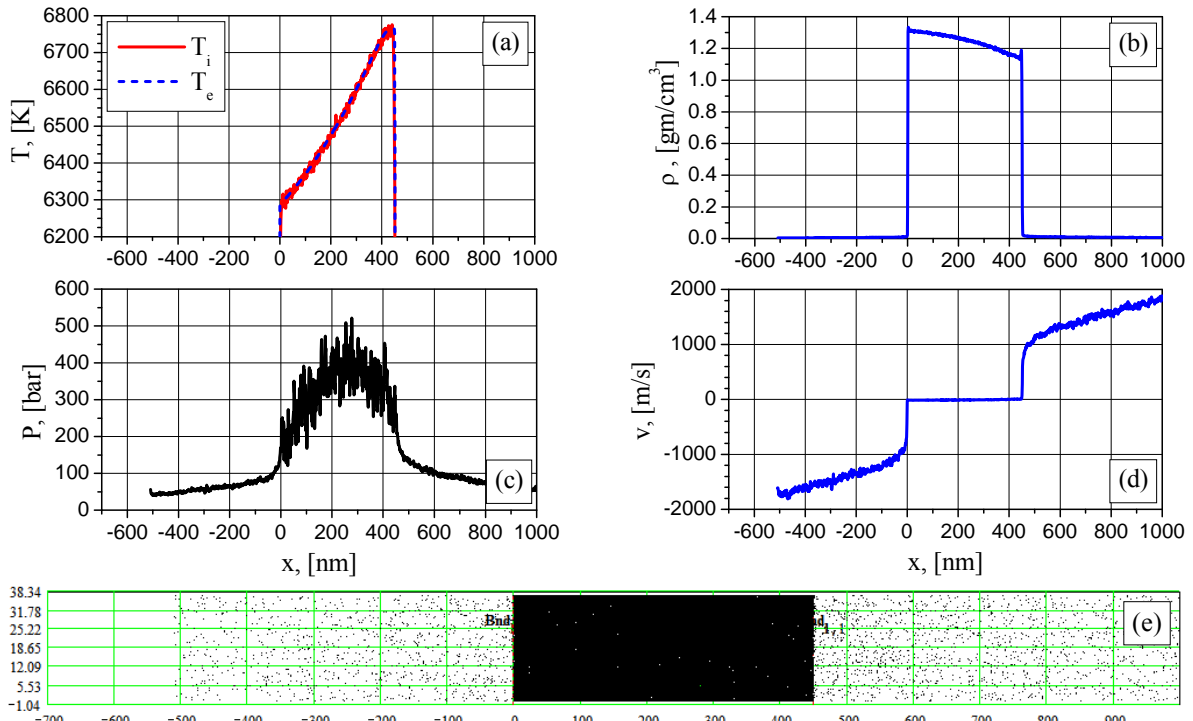


Figure 3: 1D distributions of electron (blue) and ion (red) temperature (a), density (b), pressure (c), particle velocity (d) and 2D density particle distribution (snapshot) at the time 705 ps

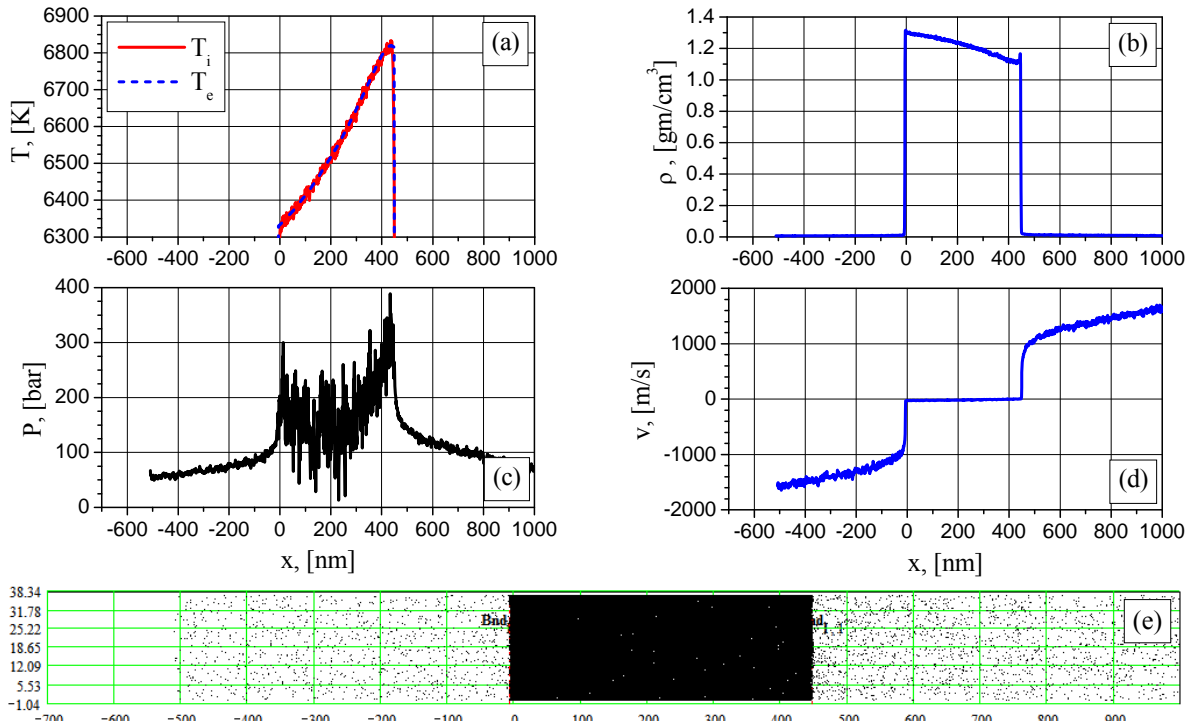


Figure 4: 1D distributions of electron (blue) and ion (red) temperature (a), density (b), pressure (c), particle velocity (d) and 2D density particle distribution (snapshot) at the time 1020 ps

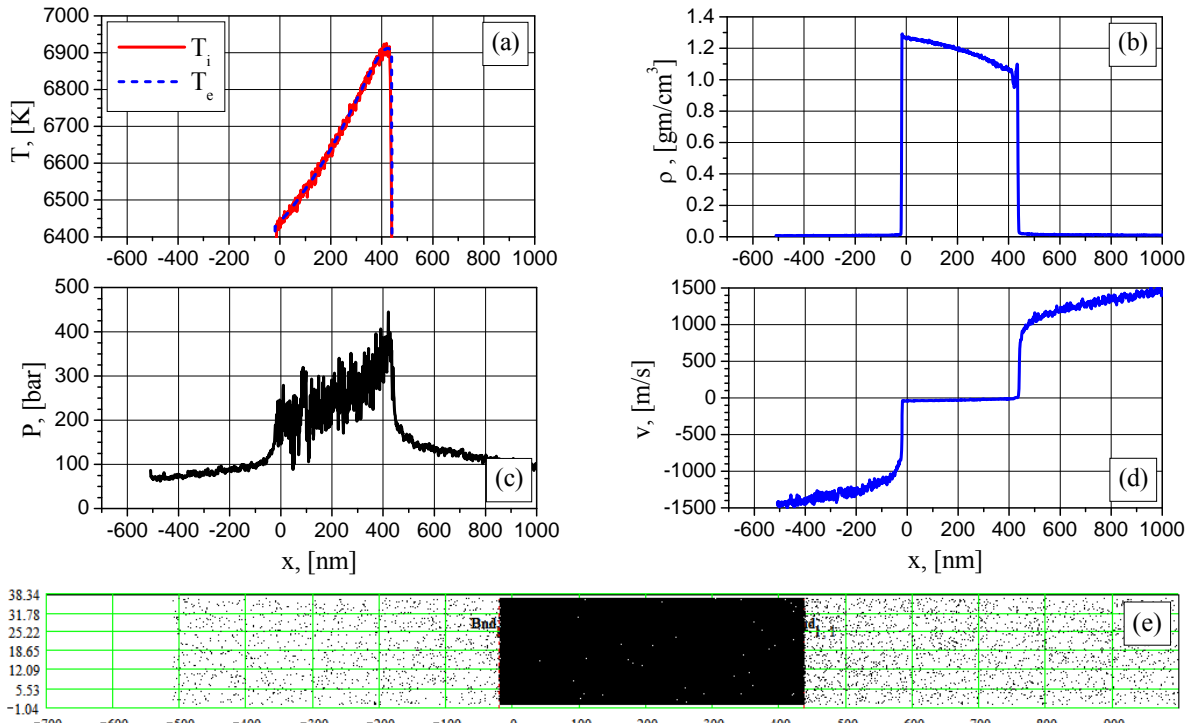


Figure 5: 1D distributions of electron (blue) and ion (red) temperature (a), density (b), pressure (c), particle velocity (d) and 2D density particle distribution (snapshot) at the time 1590 ps

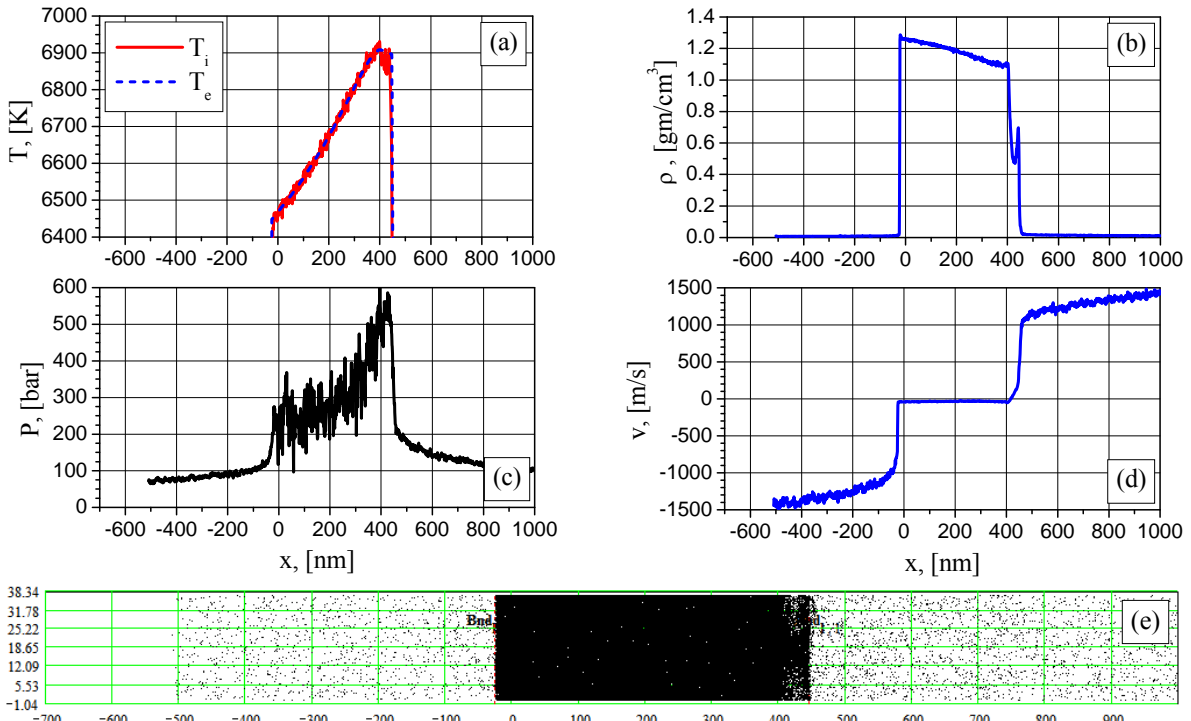


Figure 6: 1D distributions of electron (blue) and ion (red) temperature (a), density (b), pressure (c), particle velocity (d) and 2D density particle distribution (snapshot) at the time 1740 ps

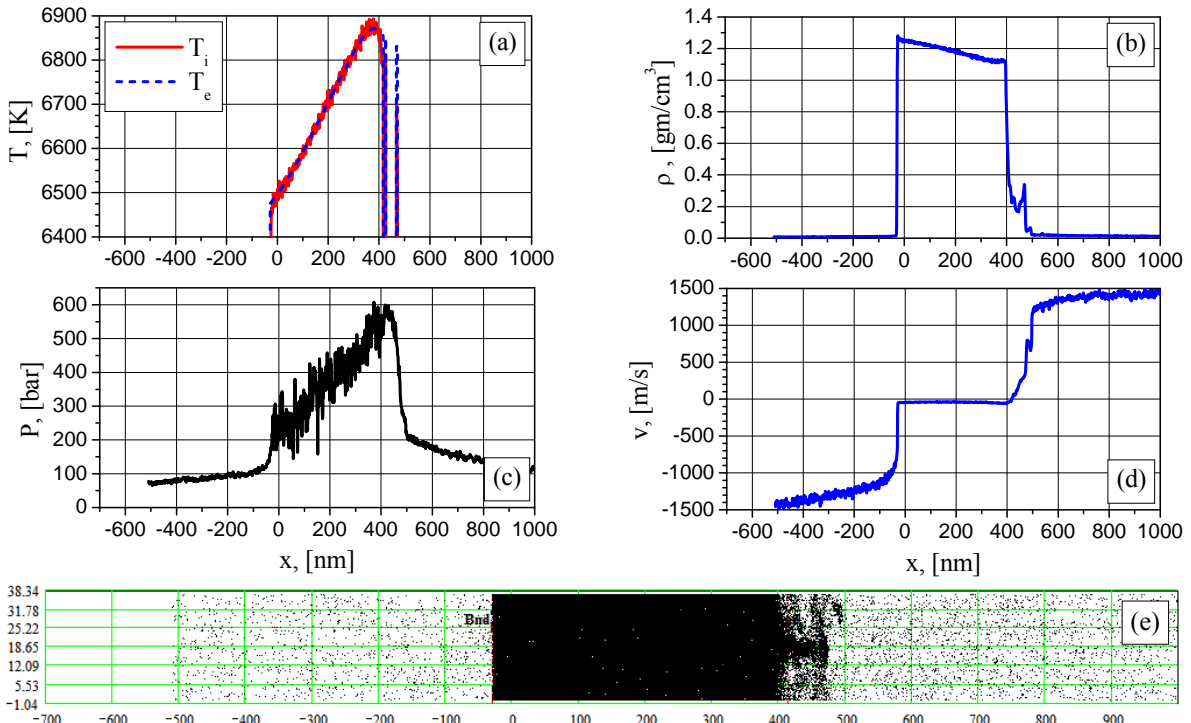


Figure 7: 1D distributions of electron (blue) and ion (red) temperature (a), density (b), pressure (c), particle velocity (d) and 2D density particle distribution (snapshot) at the time 1875 ps

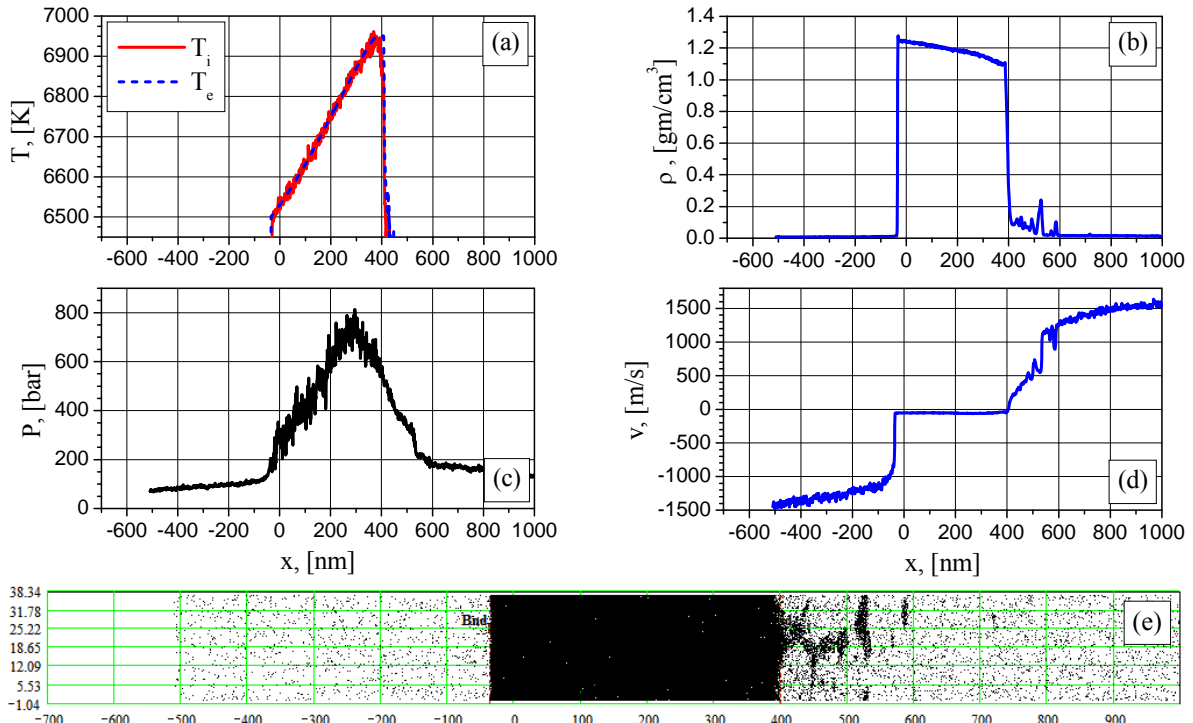


Figure 8: 1D distributions of electron (blue) and ion (red) temperature (a), density (b), pressure (c), particle velocity (d) and 2D density particle distribution (snapshot) at the time 2025 ps

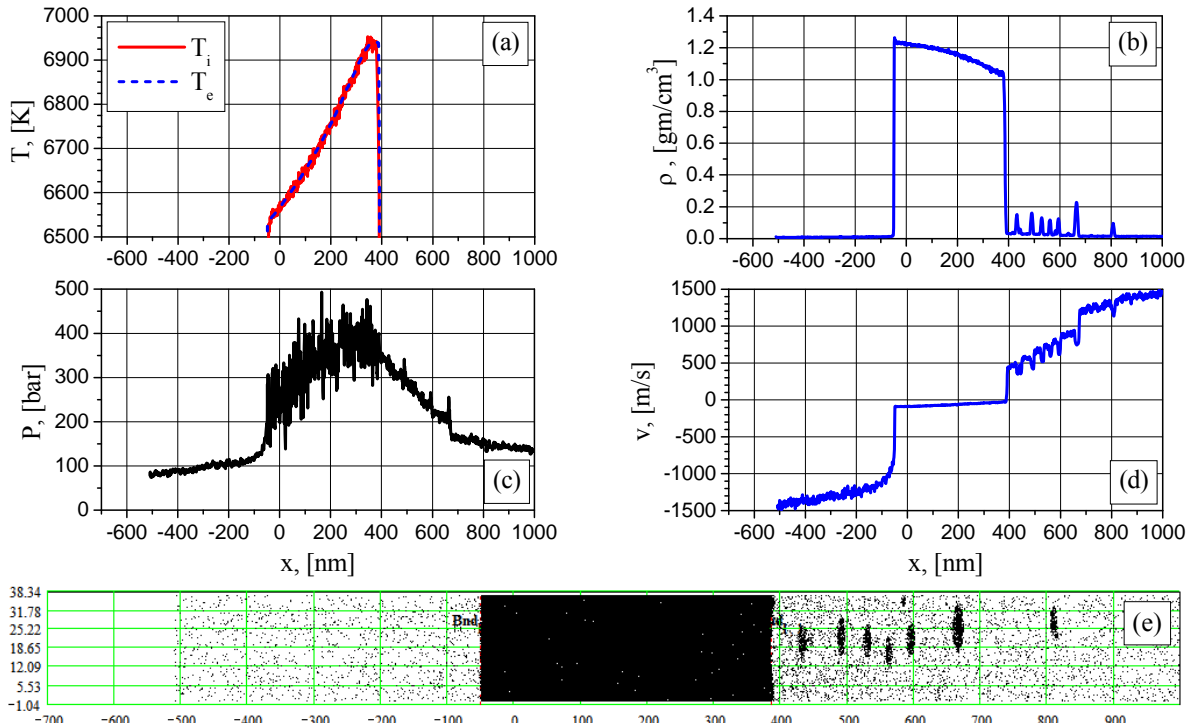


Figure 9: 1D distributions of electron (blue) and ion (red) temperature (a), density (b), pressure (c), particle velocity (d) and 2D density particle distribution (snapshot) at the time 2250 ps

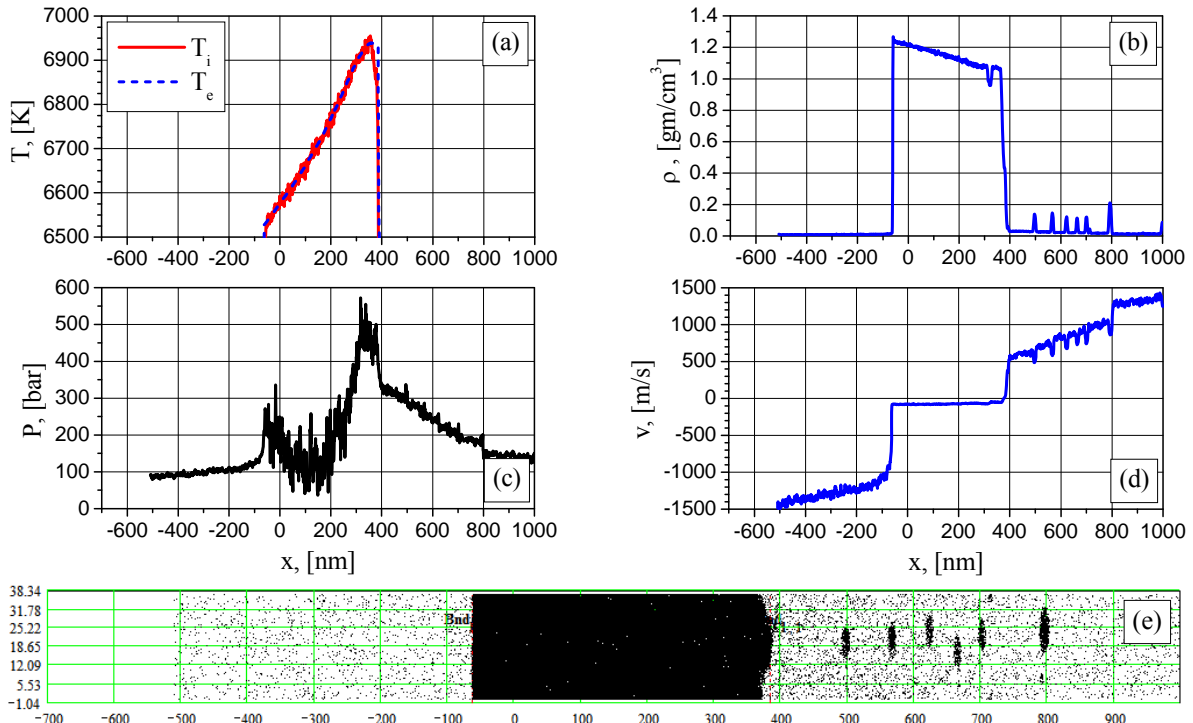


Figure 10: 1D distributions of electron (blue) and ion (red) temperature (a), density (b), pressure (c), particle velocity (d) and 2D density particle distribution (snapshot) at the time 2415 ps

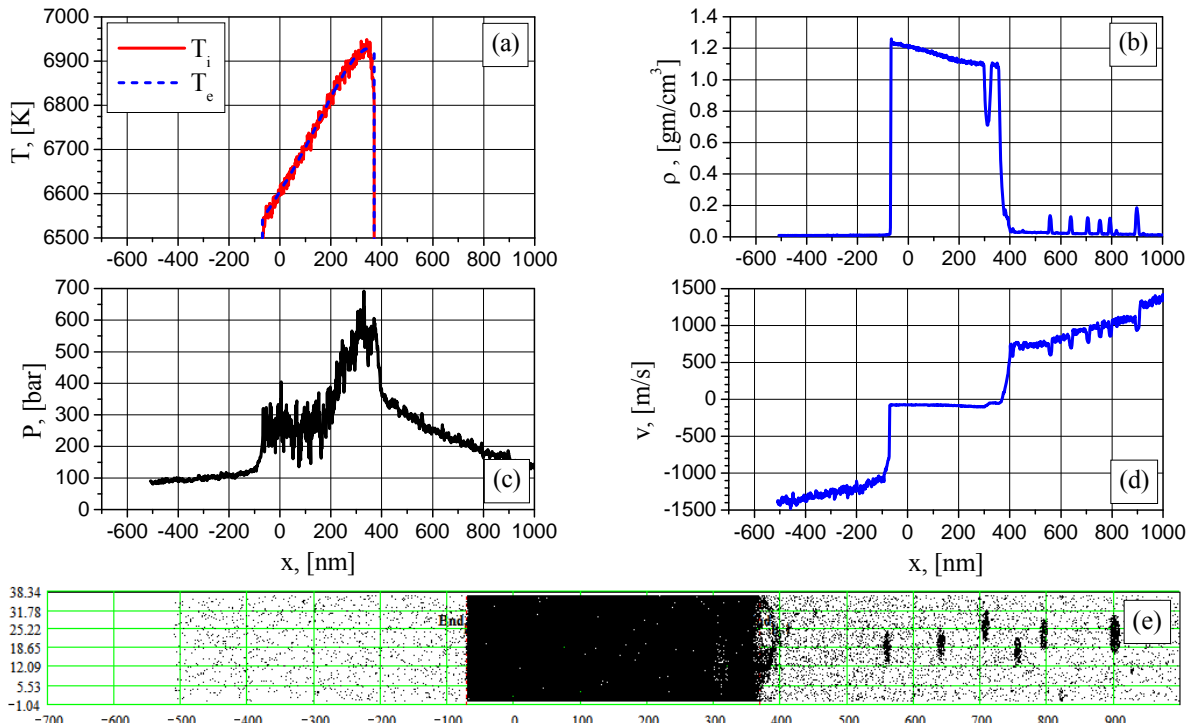


Figure 11: 1D distributions of electron (blue) and ion (red) temperature (a), density (b), pressure (c), particle velocity (d) and 2D density particle distribution (snapshot) at the time 2535 ps

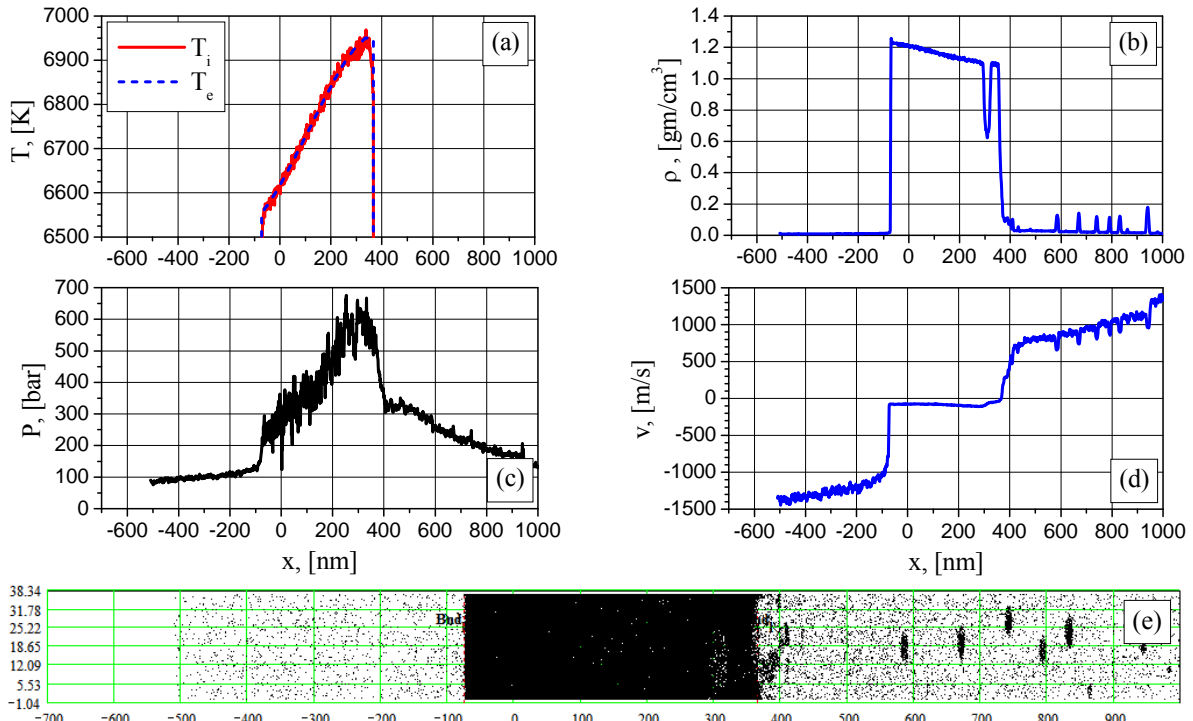


Figure 12: 1D distributions of electron (blue) and ion (red) temperature (a), density (b), pressure (c), particle velocity (d) and 2D density particle distribution (snapshot) at the time 2580 ps

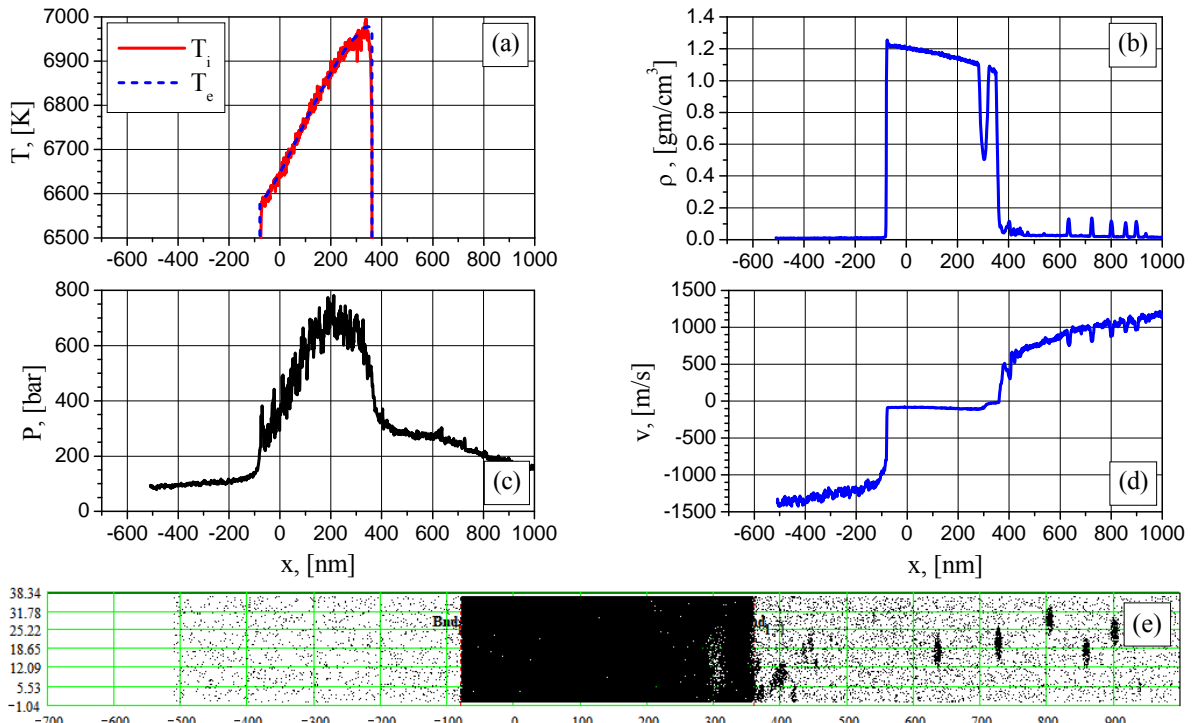


Figure 13: 1D distributions of electron (blue) and ion (red) temperature (a), density (b), pressure (c), particle velocity (d) and 2D density particle distribution (snapshot) at the time 2655 ps

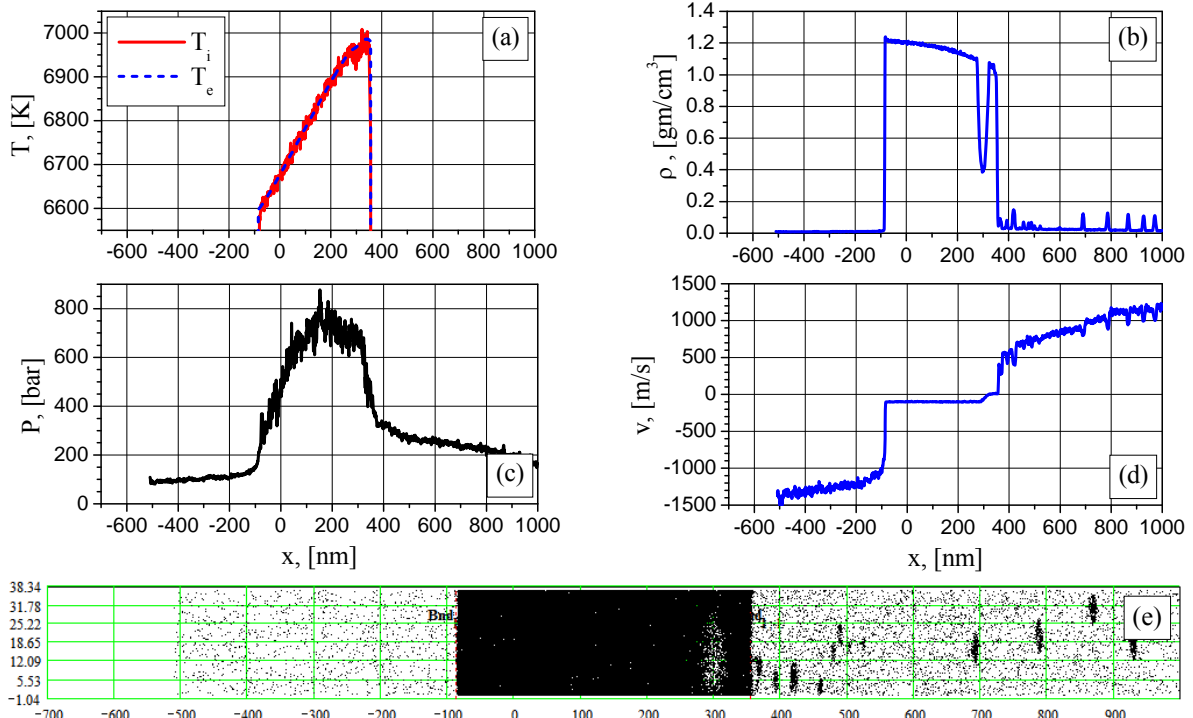


Figure 14: 1D distributions of electron (blue) and ion (red) temperature (a), density (b), pressure (c), particle velocity (d) and 2D density particle distribution (snapshot) at the time 2730 ps

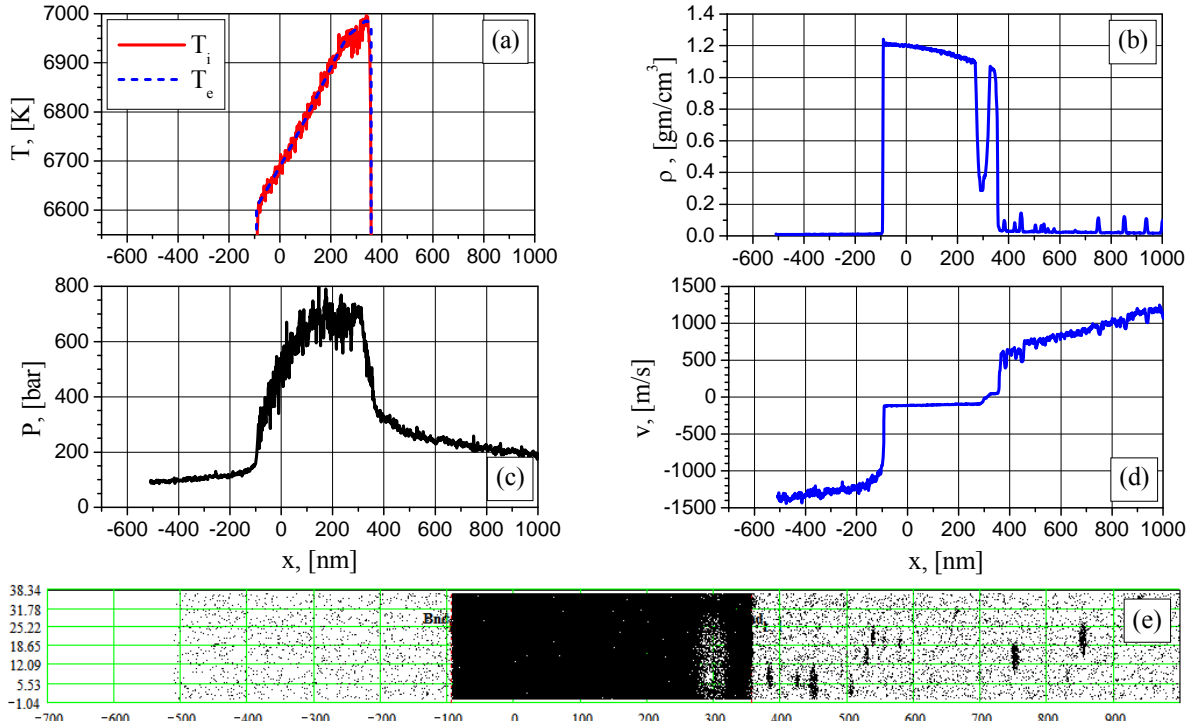


Figure 15: 1D distributions of electron (blue) and ion (red) temperature (a), density (b), pressure (c), particle velocity (d) and 2D density particle distribution (snapshot) at the time 2805 ps

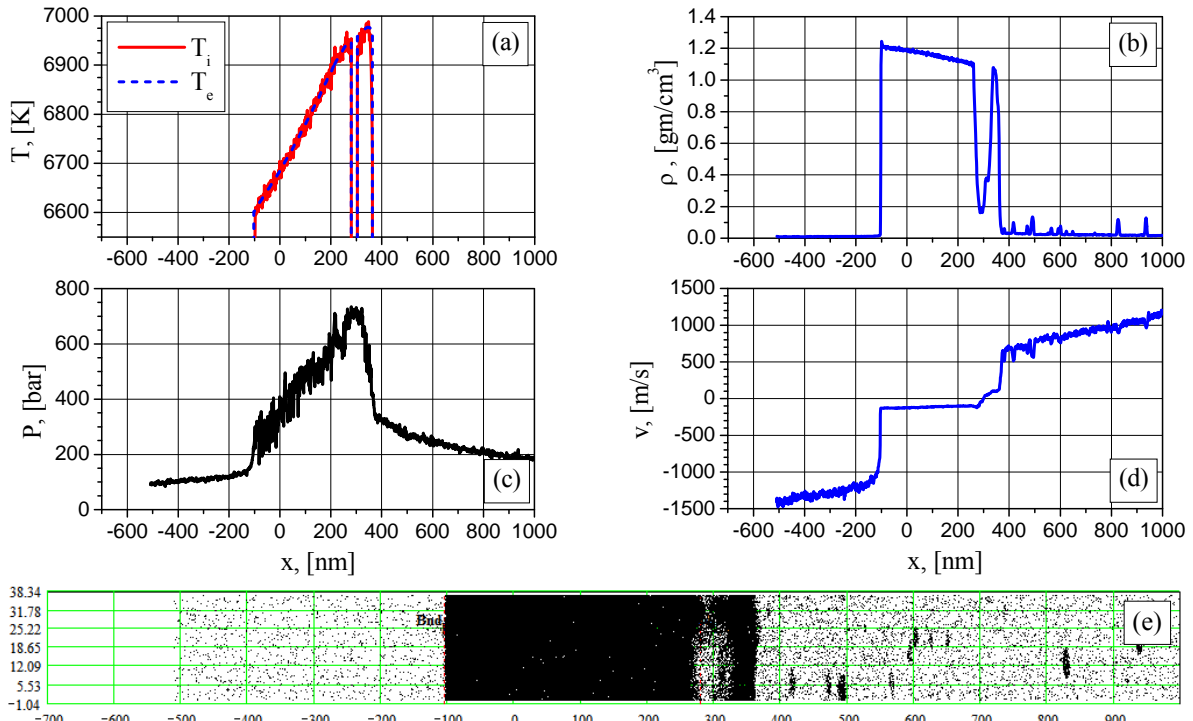


Figure 16: 1D distributions of electron (blue) and ion (red) temperature (a), density (b), pressure (c), particle velocity (d) and 2D density particle distribution (snapshot) at the time 2895 ps

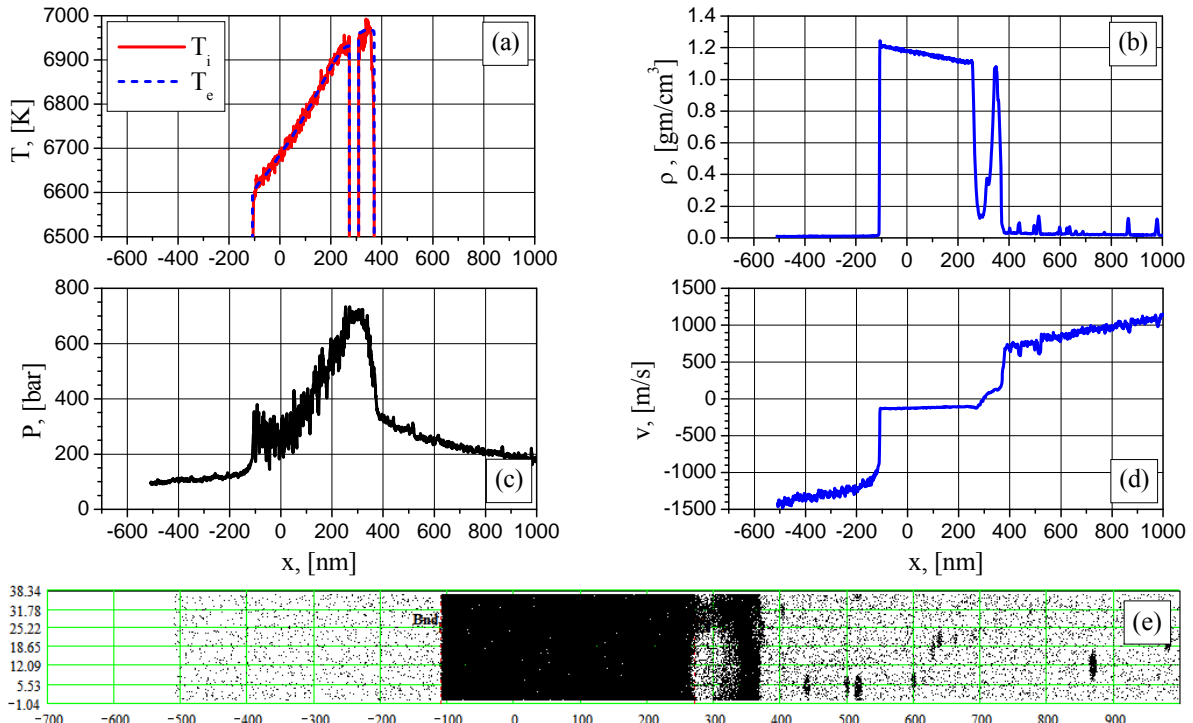


Figure 17: 1D distributions of electron (blue) and ion (red) temperature (a), density (b), pressure (c), particle velocity (d) and 2D density particle distribution (snapshot) at the time 2940 ps

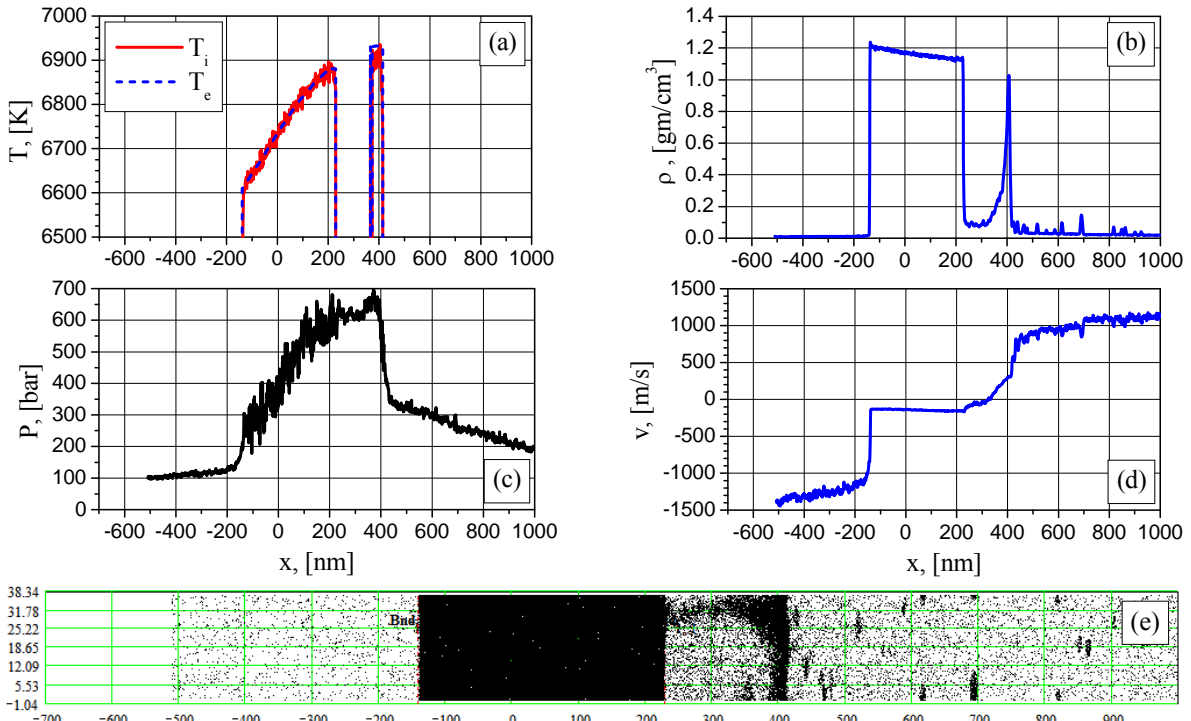


Figure 18: 1D distributions of electron (blue) and ion (red) temperature (a), density (b), pressure (c), particle velocity (d) and 2D density particle distribution (snapshot) at the time 3195 ps

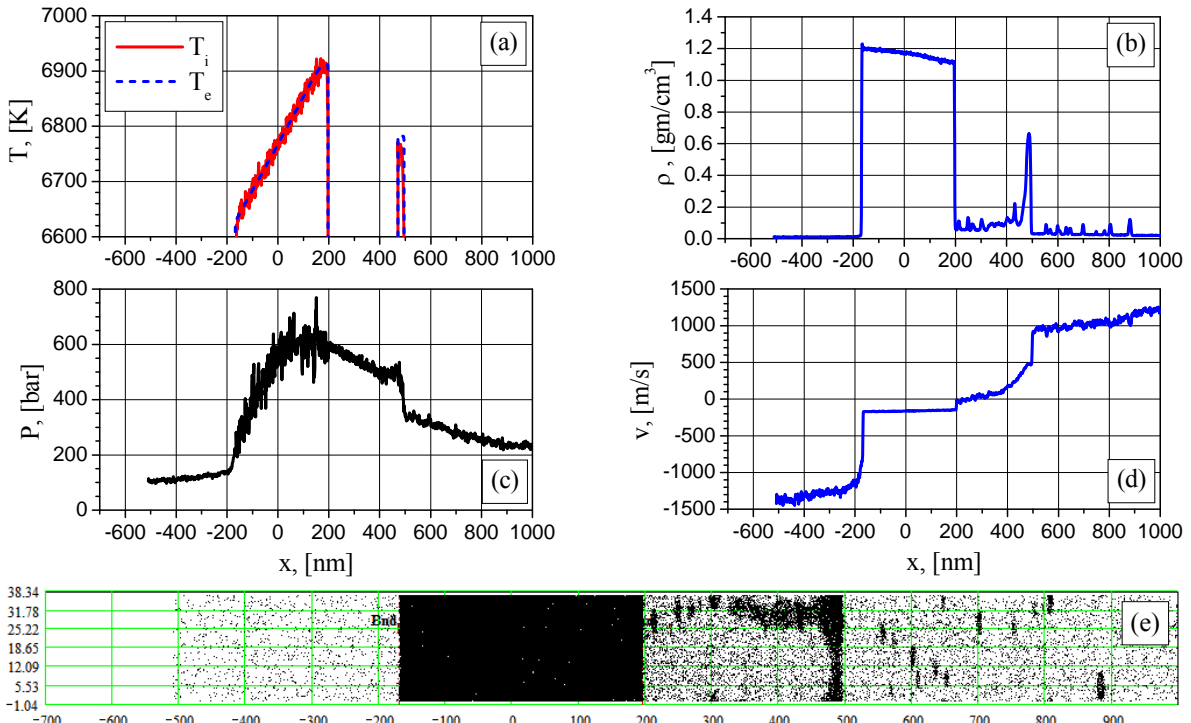


Figure 19: 1D distributions of electron (blue) and ion (red) temperature (a), density (b), pressure (c), particle velocity (d) and 2D density particle distribution (snapshot) at the time 3405 ps

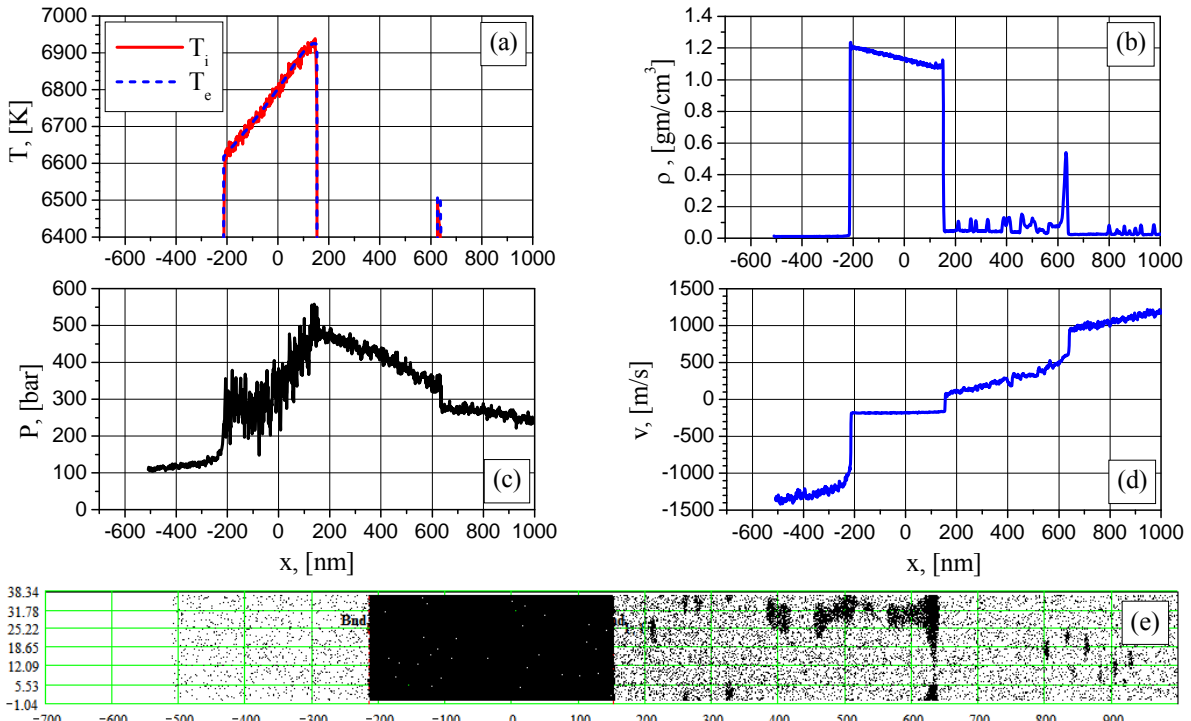


Figure 20: 1D distributions of electron (blue) and ion (red) temperature (a), density (b), pressure (c), particle velocity (d) and 2D density particle distribution (snapshot) at the time 3675 ps

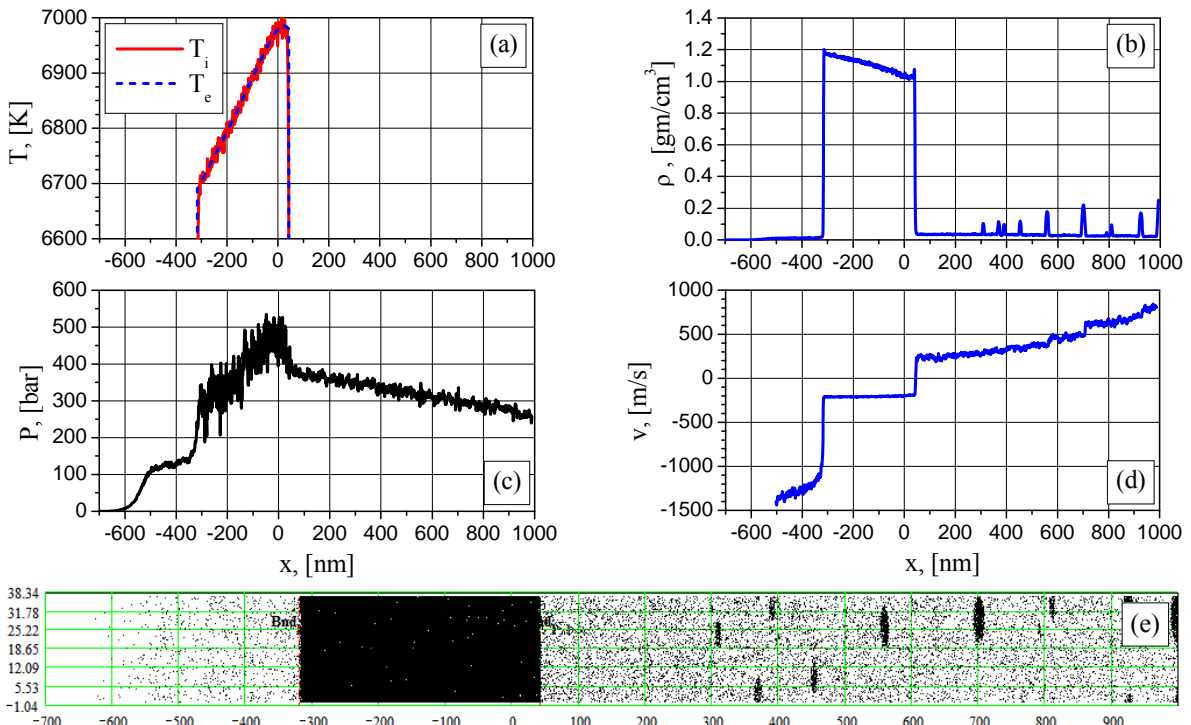


Figure 21: 1D distributions of electron (blue) and ion (red) temperature (a), density (b), pressure (c), particle velocity (d) and 2D density particle distribution (snapshot) at the time 4230 ps

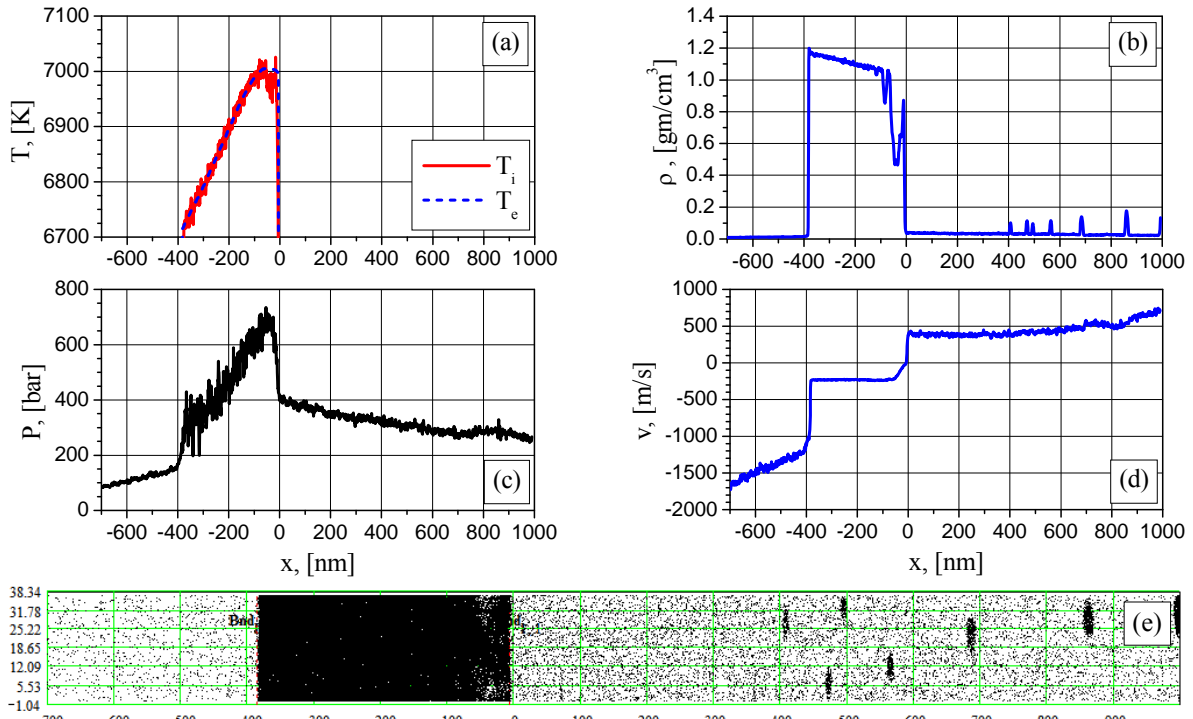


Figure 22: 1D distributions of electron (blue) and ion (red) temperature (a), density (b), pressure (c), particle velocity (d) and 2D density particle distribution (snapshot) at the time 4545 ps

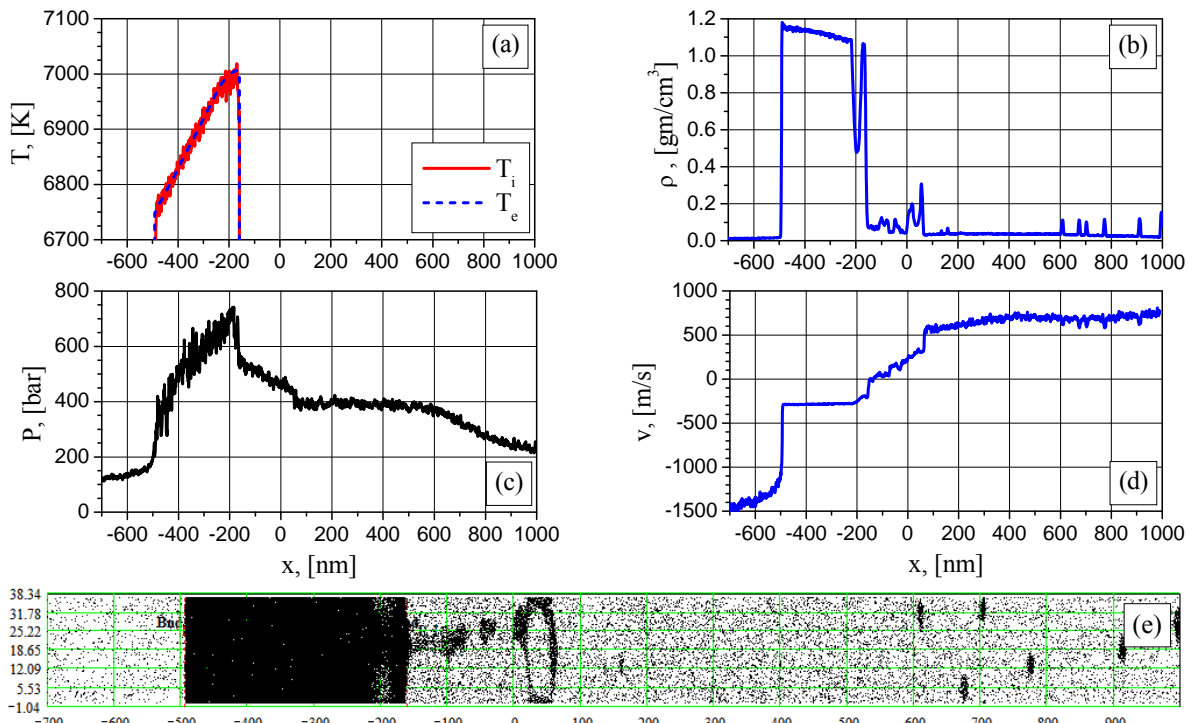


Figure 23: 1D distributions of electron (blue) and ion (red) temperature (a), density (b), pressure (c), particle velocity (d) and 2D density particle distribution (snapshot) at the time 4995 ps

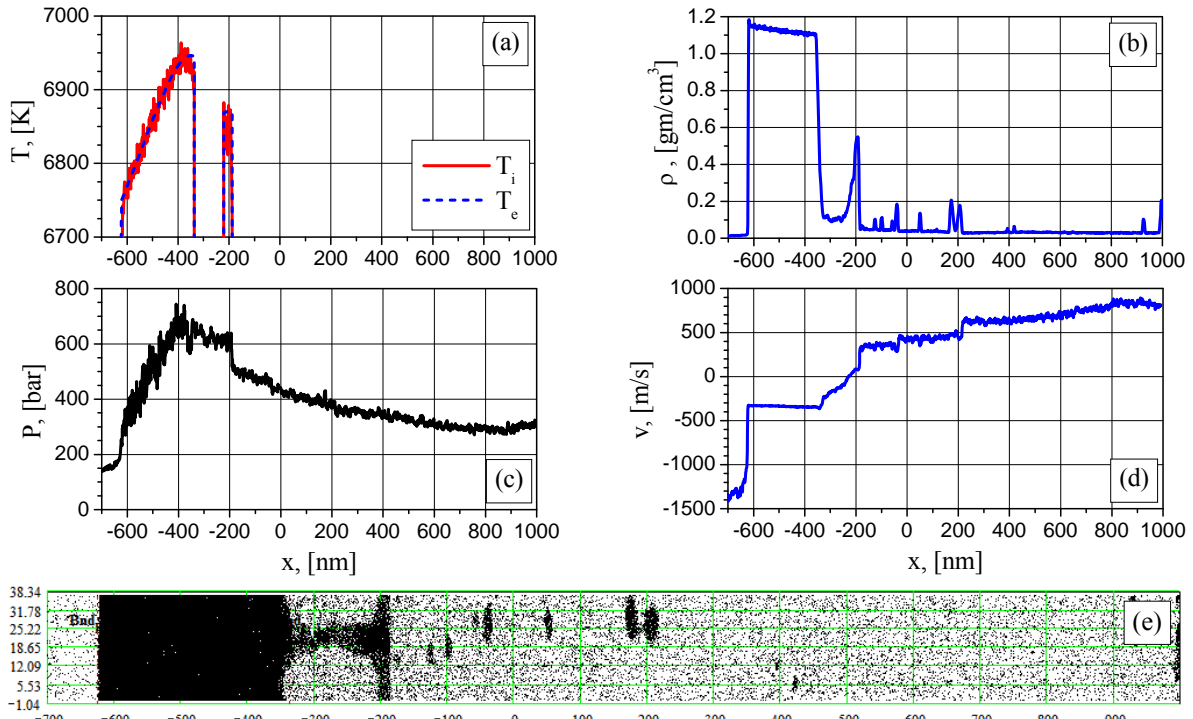


Figure 24: 1D distributions of electron (blue) and ion (red) temperature (a), density (b), pressure (c), particle velocity (d) and 2D density particle distribution (snapshot) at the time 5430 ps

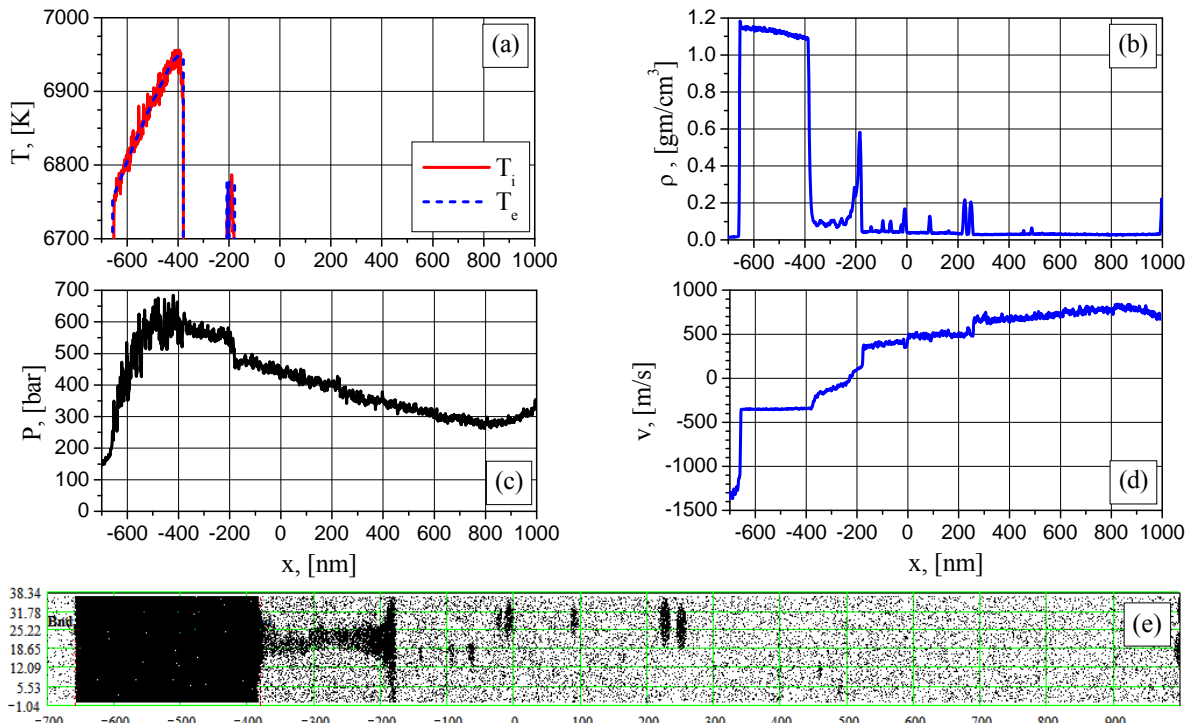


Figure 25: 1D distributions of electron (blue) and ion (red) temperature (a), density (b), pressure (c), particle velocity (d) and 2D density particle distribution (snapshot) at the time 5535 ps

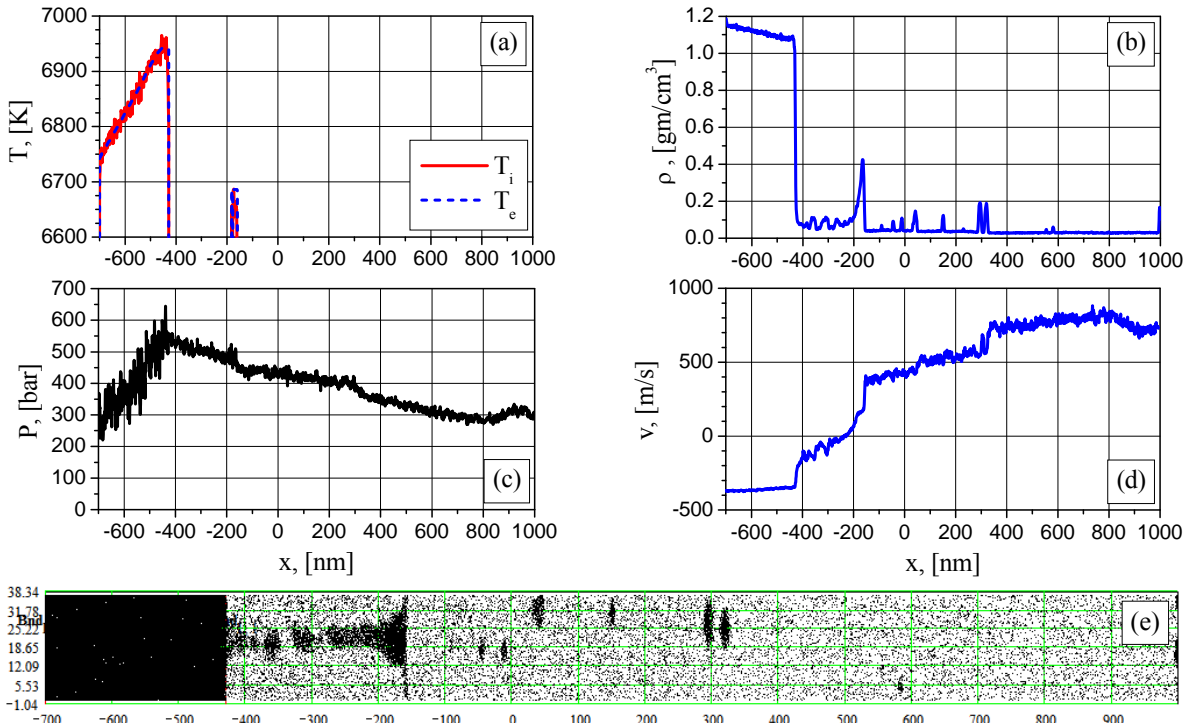


Figure 26: 1D distributions of electron (blue) and ion (red) temperature (a), density (b), pressure (c), particle velocity (d) and 2D density particle distribution (snapshot) at the time 5670 ps

## 4 CONCLUSIONS

Results obtained in the present paper show that at sufficiently intense and long laser action there is no stable stationary ablation regime determined by surface evaporation. Instead of the such regime the repetitive explosive boilings occur at the moments  $t = 1740, 2655, 4545$  and  $4995$  ps. The results qualitatively confirm previous conclusion obtained for the sample with smaller y-z periodical dimensions [14] where for  $I = 38.5 \text{ MW}/\text{cm}^2$  similar explosive boiling occur at  $t = 1040, 1440, 1640, 2000, 2340$  ps. Bigger space-dimensions and irradiated time duration considered in the present paper permit to observe more space-time inhomogeneities of the ablation process compared with the smaller sample. The results for the case of nanosecond laser ablation at higher intensities will be presented later.

The work was supported by the RSF grants № 15-11-00032.

## REFERENCES

- [1] V.V. Zhakhovskii and S.I. Anisimov. "Molecular-dynamics simulation of evaporation of a liquid", *JETP*, **84**(4), 734-745 (1997).
- [2] L.V. Zhigilei and B.J. Garrison. "Microscopic mechanisms of laser ablation of organic solids in the thermal and stress confinement irradiation regimes", *J. Appl. Phys.*, **88**, 1281-1298 (2000).
- [3] L.V. Zhigilei and E. Leveugle, B.J. Garrison, Y.G. Yingling, M.I. Zeifman. "Computer simulations of laser ablation of molecular substrates", *Chem. Rev.*, **103**, 321-347 (2003).
- [4] D.S. Ivanov and L.V. Zhigilei. "Combined atomistic-continuum modeling of short-pulse laser

- melting and disintegration of metal films”, *Phys. Rev. B*, **68**, 064114 (2003).
- [5] L.V. Zhigilei, Z. Lin, D.S. Ivanov. “Molecular dynamics study of short-pulse laser melting, recrystallization, spallation, and ablation of metal targets”, *Proceedings of IMECE2006*, Chicago, 16305 (2006).
- [6] L.V. Zhigilei, Z. Lin, D.S. Ivanov. “Atomistic modeling of short pulse laser ablation of metals: connections between melting, spallation, and phase explosion”, *J. Phys. Chem. C*, **113**, 11892–11906 (2009).
- [7] E.T. Karim, Z. Lin, L.V. Zhigilei. “Molecular dynamics study of femtosecond laser interactions with Cr targets”, *AIP Conf. Proc.*, **1464**, 280-293 (2012).
- [8] C. Wu, L.V. Zhigilei. “Microscopic mechanisms of laser spallation and ablation of metal targets from large-scale molecular dynamics simulations”, *Appl. Phys. A*, **114**, 11–32 (2014).
- [9] N.A. Inogamov, V.V. Zhakhovsky, V.A. Khokhlov, K.V. Khishchenko, Y.V. Petrov, D.K. Il'nitsky, K.P. Migdal. “Geometrical constrains and femtosecond laser ablation”, *Physical-Chemical Kinetics in Gas Dynamics*, **15**(5), 1-33 (2014).
- [10] S. Zhang, F. Hao, H. Chen, W. Yuan, Y. Tang, X. Chen. “Molecular dynamics simulation on explosive boiling of liquid argon film on copper nanochannels”, *Applied Thermal Engineering*, **113**(25), 208–214 (2017).
- [11] A. Mazzi, A. Miotello. “Simulation of phase explosion in the nanosecond laser ablation of aluminum”, *Journal of Colloid and Interface Science* (2016), doi: 10.1016/j.jcis.2016.08.016
- [12] V.I. Mazhukin, A.A. Samokhin, M.M. Demin, A.V. Shapranov. “Explosive boiling of metals upon irradiation by a nanosecond laser pulse”, *Quantum Electronics*, **44**(4), 283-285 (2014).
- [13] V.I. Mazhukin, A.V. Shapranov, A.A. Samokhin, A.Yu. Ivochkin. “Mathematical modeling of non-equilibrium phase transition in rapidly heated thin liquid film”, *Mathematica Montisnigri*, **27**, 65-90 (2013).
- [14] V.I. Mazhukin, A.A. Samokhin, M.M. Demin, A.V. Shapranov. “Modeling of nanosecond laser vaporization and explosive boiling of metals”, *Mathematica Montisnigri*, **29**, 68-90 (2014).
- [15] V.I. Mazhukin, A.V. Shapranov, O.N. Koroleva, A.V. Rudenko. “Molecular dynamics simulation of critical point parameters for silicon”, *Mathematica Montisnigri*, **31**, 64-77 (2014).
- [16] V.I. Mazhukin, A.A. Samokhin, A.V. Shapranov, M.M. Demin, P.A. Pivovarov. “On different regimes of condensed matter ablation depending on intensity and duration of absorbed electromagnetic pulses”, *PIERS Proceedings*, Prague, 2418-2421 (2015).
- [17] V.I. Mazhukin, A.A. Samokhin, A.V. Shapranov, M.M. Demin. “Modeling of thin film explosive boiling—surface evaporation and electron thermal conductivity effect”, *Mater. Res. Express*, **2**, 016402 (2015).
- [18] M.I. Kaganov, I.M. Lifshitz, L.V. Tanatarov. Relaxation between electrons and the crystalline lattice, *JETP*, **4**(2), 173-178 (1957).
- [19] I.M. Lifshitz, M.I. Kaganov, L.V. Tanatarov. “K teorii radiacionnyh izmenenij v metallah”, *At. Energ.*, **6**, 391-402 (1959).
- [20] S.I. Anisimov, B.L. Kapeliovich, T.L. Perelman. “Electron emission from metal surfaces exposed to ultrashort laser pulses”, *Sov. Phys. JETP*, **39**(2), 375-377 (1974).
- [21] L.D. Landau, E.M. Lifshitz. *Statistical Physics*, Butterworth-Heinemann. Vol.5 (3rd ed.), (1980).
- [22] G.V. Gordeev. “Low-frequency plasma vibrations”, *JETP*, **27**, 19-23 (1954).
- [23] V.I. Mazhukin. “Kinetics and Dynamics of Phase Transformations in Metals Under Action of

- Ultra-Short High-Power Laser Pulses. Chapter 8”, *In Laser Pulses – Theory, Technology, and Applications*, InTech., ed. by I. Peshko., 219-276 (2012).
- [24] V.V. Zhakhovskii, N.A. Inogamov, Yu.V. Petrov, S.I. Ashitkov, K. Nishihara “Molecular dynamics simulation of femtosecond ablation and spallation with different interatomic potentials”, *Appl. Surf. Sci.*, **255**, 9592 (2009).

*The results were presented at the 15-th International seminar "Mathematical models & modeling in laser-plasma processes & advanced science technologies" (September 26 -October 1, 2016, Petrovac, Montenegro).*

Received August, 5 2016.